

Giant conductivity enhancement: Pressure-induced semiconductor-metal phase transition in $\text{Cd}_{0.90}\text{Zn}_{0.1}\text{Te}$

H. Saqib,^{1,2} S. Rahman,² D. Errandonea,³ Resta A. Susilo,² A. Jorge-Montero,⁴ P. Rodríguez-Hernández,⁴ A. Muñoz,⁴ Yan Sun,¹ Zhiqiang Chen,² Ning Dai,^{1,*} and Bin Chen^{2,†}

¹Shanghai Institute of Technical Physics, Chinese Academy of Science, Shanghai 201800, China

²Center for High Pressure Science and Technology Advanced Research, Shanghai 201203, China

³Departamento de Física Aplicada-ICMUV, MALTA Consolider Team, Universidad de Valencia, Edificio de Investigación, C/Dr. Moliner 50, Burjassot, 46100 Valencia, Spain

⁴Departamento de Física and Instituto de Materiales y Nanotecnología, Universidad de La Laguna San Cristóbal de La Laguna, 31201 Tenerife, Spain



(Received 25 December 2018; revised manuscript received 6 February 2019; published 21 March 2019)

Element doping and pressure compression may change material properties for improved performance in applications. We report pressure-induced metallization in the semiconductor $\text{Cd}_{0.90}\text{Zn}_{0.1}\text{Te}$. Transport measurements showed an overall resistivity drop of 11 orders of magnitude under compression up to 12 GPa, which is indicative of a metallization transition. X-ray diffraction measurements revealed that the sample underwent a structural transition from a cubic- $F4\bar{3}m$ phase (zinc blende) to a cubic- $Fm\bar{3}m$ phase (rock salt) at about 5.5 GPa, followed by another transition to an orthorhombic $Cmcm$ structure at 13 GPa. A huge volume collapse of about 18% was observed during the first phase transition, suggesting a first-order phase transition. The disappearance or weakening of Raman modes, temperature-dependent resistivity, and *ab initio* calculation results depict the metallic nature of both the rock-salt and $Cmcm$ phases. The band structure changes and increased carrier density (especially at the first structural transition) are likely a consequence of the structural transition.

DOI: [10.1103/PhysRevB.99.094109](https://doi.org/10.1103/PhysRevB.99.094109)

I. INTRODUCTION

Binary and ternary semiconductor alloys (TSAs), consisting of II-VI elements, exhibit excellent optical, thermodynamic, and electronic properties with a wide range of applications in optoelectronic detectors, phase change memory devices, and thermoelectric generators [1–3]. Among these systems, CdTe is one of the most popular binary chalcogenides with diverse technological applications including medical imaging, environmental monitoring, as well as x-ray and gamma-ray detectors [4–6]. Structural stability and transformation processes are critical to the development of the materials for various applications. Moreover, the broad applications of the materials demand a way to tune their electronic properties over a wide range. For example, for the materials to be applied in optoelectronic applications, it is necessary to tune their band gaps and carrier mobility. Most of the binary and ternary chalcogenides II-VI semiconductors, such as CdTe, $\text{Cd}_{1-x}\text{Mn}_x\text{Te}$, $\text{Cd}_{1-x}\text{Zn}_x\text{Te}$, HgTe, $\text{Zn}_{1-x}\text{Mn}_x\text{Se}$, and ZnTe, are known to exhibit polymorphic behavior under extreme conditions [7–10]. Doping can dramatically enhance the electrical and magnetic properties of Cd-based chalcogenides for their efficient use in various applications. Recently, Lukas *et al.* reported that the efficiency of solar cells could be enhanced by controlling Cu doping in CdTe [11]. Ebrahim and co-workers revealed that for cobalt-doped CdTe, the

presence of the Co^{2+} ion might create some defects or vacancy sites that play an important factor in varying the optical and magnetic properties of CdTe, which is useful for spintronics applications [12].

$\text{Cd}_{1-x}\text{Zn}_x\text{Te}$, the alloy of CdTe in ZnTe, has shown novel effects on the electronic properties compared with those of the parent compounds CdTe and ZnTe. $\text{Cd}_{1-x}\text{Zn}_x\text{Te}$ nuclear detectors, for instance, exhibit superior performance. It has a sensitivity advantage over conventional ones (e.g., HgI_2 detectors) of between two and three orders of magnitude, providing a cost-efficient alternative for the conventional semiconductor x-ray detectors. Moreover, gamma-ray cameras based on $\text{Cd}_{1-x}\text{Zn}_x\text{Te}$ are now an essential part of the new generation of nuclear medicine. Unlike both CdTe and ZnTe, the $\text{Cd}_{1-x}\text{Zn}_x\text{Te}$ compound exhibits ferroelectricity. Weil *et al.* reported for the first time that the origin of ferroelectricity in $\text{Cd}_{1-x}\text{Zn}_x\text{Te}$ is due to the differences in their cationic size [13]. Although the ionic radius of Zn^{2+} (0.74 Å) is smaller than that of Cd^{2+} (0.95 Å), Zn ions can replace Cd ions, thereby reducing their electric anisotropy, and control the structural stability. Other than doping effects, the electronic properties, in particular the band gap of TSAs, can be tuned by changing the chemical composition, temperature, and pressure [14]. In the past, several attempts have been made to tune the band gap of TSAs by controlling the particle's size, varying the amount of constituents and temperature [15,16]. While these methods can be used to tune the properties of these materials, they are shown to be ineffective and possess a number of disadvantages, one of which is the lack of ability to tune the electronic properties reversibly [17].

*Corresponding author: ndai@mail.sitp.ac.cn

†chenbin@hpstar.ac.cn

A high-pressure investigation for the parent compound CdTe has been previously documented [7,18]. A direct zinc-blende to rock-salt (ZB-RS) transition was initially reported at about 3.5 GPa by Mariano *et al.* [19]; however, it was later found that the transition occurred via an intermediate cinnabar phase in a small region of pressure (2.7 to 3.5 GPa) [20]. However, Gilliland *et al.* do not report any discontinuity in the energy gap in the narrow pressure range where this phase can be present [21]. The most widely accepted pressure sequence today in CdTe is from the ZB phase to cinnabar and then to the RS phase, and a further transition to the *Cmcm* phase was reported by Nemes *et al.* [7].

Solid alloys (such as $\text{Cd}_{0.90}\text{Zn}_{0.1}\text{Te}$) do not always behave similarly to any of the end members, as generally assumed. The difference in behavior can already be inferred from the observation of ferroelectricity in $\text{Cd}_{1-x}\text{Zn}_x\text{Te}$, but not in CdTe and ZnTe [13]. Hence, the high-pressure behaviors in $\text{Cd}_{0.9}\text{Zn}_{0.1}\text{Te}$ might be expected to be different. However, the absence of any high-pressure studies renders our understanding of whether the Zn-doped CdTe will possess different or similar high-pressure properties than the parent compound CdTe. Our particular aim is to elucidate the phase stability and changes in electronic properties in response to both the cation substitution and application of pressure in CdTe. In the current study, we investigated the combined effect of pressure and composition on the properties of CdTe.

We found two phase transformation pressure points at nearly 5 and 13 GPa. High-pressure studies on the undoped CdTe revealed a five-order resistivity drop in previous studies [22,23]. However, in our case, there is an overall nine-order resistivity drop from ambient to 5.5 GPa where a six-order sharp drop was seen at the first phase transition. This huge resistivity decrease was associated with a semiconductor-to-metal phase transition. A second phase transition at 13 GPa was a metal-to-metal phase transition. Importantly, the phase transitions are reversible, as confirmed by experimental and theoretical high-pressure (HP) x-ray diffraction (XRD) and HP Raman results. Comparing with the high-pressure properties of CdTe, the structural and electronic transition pressures of $\text{Cd}_{0.9}\text{Zn}_{0.1}\text{Te}$ seem to be higher, whereas the magnitude of the resistivity drops is much higher than that of the parent compounds CdTe, which indicates that the cationic substitutions lead to improved stability of the crystal structure that facilitates the transition at relatively higher pressure.

II. EXPERIMENT

The sample $\text{Cd}_{0.9}\text{Zn}_{0.1}\text{Te}$ was prepared by the well-known Bridgman method [24]. We used the powder sample for all our experiments. The *in situ* high-pressure electrical resistivity of $\text{Cd}_{0.9}\text{Zn}_{0.1}\text{Te}$ was measured by the standard four-probe technique in a diamond-anvil cell (DAC) up to 40 GPa. The sample resistivity can be calculated according to the van der Pauw formula [25]. The thickness of the sample under high pressure was determined using a micrometer with a precision of 0.5 μm . A mixture of epoxy and cubic boron nitride was utilized as the coating on the steel gaskets to ensure electrical insulation between different electrodes. Four platinum electrodes and copper wires were set up to contact the sample in the chamber. No pressure medium was used for the HP

electrical resistance measurement. The data was obtained using a 4050 Keithley precise source measuring unit at room temperature (RT). In the rest of the experiments, the pressure was generated with a symmetric DAC using a steel gasket and silicone oil as the pressure transmitting medium. The ruby fluorescence method was employed for pressure calibration [26]. At room temperature, HP XRD experiments of the samples were measured at the Advanced Light Source (ALS) (BL 12.2.2 beam line), Lawrence Berkeley National Lab (LBNL), with an x-ray wavelength of 0.4959 Å. The two-dimensional x-ray diffraction images were collected by a charge coupled device (CCD) detector. These two-dimensional ring-type images were integrated using FIT2D software and the structure was evaluated by FULLPROF software [27]. The Raman spectra were collected by a Renishaw InVia Spectrometer system with laser wavelengths of 532 nm and 785 nm with gratings of 2400 and 1200 grooves/cm, respectively. The wave numbers of the Raman peaks were determined with an accuracy of 1 cm^{-1} .

Ab initio calculation. Structural and band structure first-principles simulations were performed using the density functional theory (DFT) [28], as implemented in ABINIT [29]. We used the virtual crystal approximation to describe $\text{Cd}_{0.9}\text{Zn}_{0.1}\text{Te}$. Nonlocal norm-conserving pseudopotentials [30] with a plane-wave basis set of 60 Hartree were employed. The exchange-correlation energy was included in the generalized gradient approximation, with the Perdew-Burke-Ernzerhof (PBE) [31] prescription. Brillouin zone (BZ) integrations were carried out with $4 \times 4 \times 4$ ($8 \times 8 \times 8$) Monkhorst-Pack [32] grids in the zinc-blende and rock-salt (*Cmcm*) structure. The achieved convergence in the total energy was 1 meV per formula unit, and the forces on the atoms were $< 0.001\text{ eV}/\text{Å}$. The direct method was employed using the PHONON program to study the phonon modes at the Γ point [33].

III. RESULTS

A. Electrical resistivity under high pressure

The pressure dependence of $\text{Cd}_{0.9}\text{Zn}_{0.1}\text{Te}$ resistivity was obtained up to 40 GPa. It is a semiconductor with a band gap of 1.55 eV at ambient conditions [34]. We not only observed the evolution of resistivity (ρ) with pressure (P) in $\text{Cd}_{0.9}\text{Zn}_{0.1}\text{Te}$, but also extensively studied the linear, nonlinear, and switching phenomena simultaneously by recording the dc current voltage (I-V), as shown in Fig. S3 of the Supplemental Material [35]. We observed that the electrical current increased linearly by increasing the voltage for all pressures ($\sim 0 - 40$ GPa). Figure 1(a) depicts the electrical resistivity (ρ) of $\text{Cd}_{0.9}\text{Zn}_{0.1}\text{Te}$ as a function of P at RT. The ρ of the cubic phase $\text{Cd}_{0.9}\text{Zn}_{0.1}\text{Te}$ at RT is $\sim 10^8\ \Omega\text{ cm}$, which is one order of magnitude greater than that of CdTe due to its larger band gap because Zn partially replaces Cd. For $P \leq 1.3$ GPa, in region AO, ρ increased with increasing pressure. A slight decrease in mobility can account for this initial rise in resistivity. This is consistent with our calculation based on the $\mathbf{k}\cdot\mathbf{p}$ model. It is known that the band gap opens up under compression for the zinc-blende (ZB) structure [21] (a fact also confirmed by our calculations), which according to

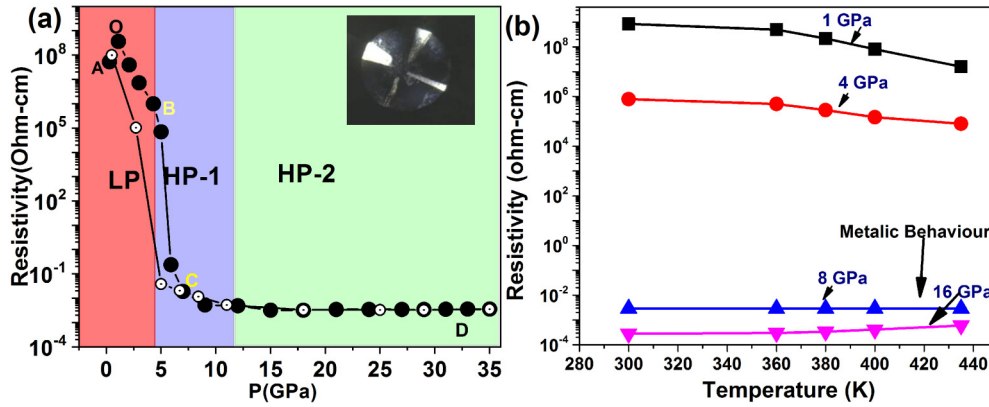


FIG. 1. (a) The variation of resistivity as a function of pressure for $\text{Cd}_{0.9}\text{Zn}_{0.1}\text{Te}$. Closed symbols represent compression data, while open symbols are for decompression data. (b) The isobaric temperature-dependent resistance of the sample at a few representative pressure values.

the $\mathbf{k}\cdot\mathbf{p}$ model will cause an increase of the effective mass, lowering the mobility [22].

In region OB (1–5 GPa), ρ decreased almost linearly with slope $d\ln(\rho)/dP \sim -0.291 \pm 0.008 \text{ GPa}^{-1}$ and reached its lower value of $3.5 \times 10^6 \Omega \text{ cm}$. This is consistent with a change in the nature of the extrinsic levels under compression even though the band gap is increasing. Also, in the low-pressure region, we cannot ignore the extrinsic effect of initially high contact resistance between the grains of the sample. Normally, $\text{Cd}_{0.9}\text{Zn}_{0.1}\text{Te}$ possesses deep levels that are not compensated and become sharper under pressure. This is a typical phenomenon that leads to the reduced self-compensation and provides carriers to the valence and conduction band. Thus, the carrier concentration will increase and will ultimately reduce the resistivity [36], as we observed.

For $P > 5 \text{ GPa}$, ρ decreased sharply in the BC region. The ZB and rock-salt (RS) phases coexist, which accounts for the further decrease of resistivity between $4.5 < P < 7.5 \text{ GPa}$. The overall change in the first high-pressure region (HP-1) was about nine orders of magnitude. The pressure dependence of ρ in the BC region was $d\ln(\rho)/dP \sim -0.634 \pm 0.011 \text{ GPa}^{-1}$. The value of resistivity at 12 GPa reached $5.2 \times 10^{-3} \Omega \text{ cm}$ and then became almost P independent at above 12 GPa in region CD. Hence, the pressure has very little effect on the conductivity of the second high-pressure region HP-2. The sudden decrease in resistivity after $\sim 5 \text{ GPa}$ could be associated with structural changes, which have also been suggested by various theoretical and experimental studies [21,37,38].

In the CD region, there were minor changes in resistivity, which is indicative of a stable metallic state. We estimated the charge density as $n_c \sim 10^{11} \text{ cm}^{-3}$ by assuming electronic mobility of $\mu \sim 10^2 \text{ cm}^2/\text{V s}$, confirming the semiconducting behavior of the material at ambient phase [22,39]. However, for HP-2 in the CD region, the charge density n_c was estimated to be $10^{22}/\text{cm}^3$, which is ten orders of magnitude larger than in the ambient phase, by assuming that μ lies in the range $1 - 10 \text{ cm}^2/\text{V s}$ [22]. Such an enhanced carrier density is a clear indication of metallization. In the decompression cycle, ρ was completely recovered with little hysteresis to $\sim 5.5 \times 10^8 \Omega \text{ cm}$. Such reversibility in the pressure tuning of the electric properties of this material has strong potential for wider practical applications.

To better understand the nature of the sample's conductivity, we measured resistivity as a function of temperature at a few fixed pressures, and the results are shown in Fig. 1(b). The slope of the temperature-dependent resistivity is negative, $d\rho/dT < 0$ for $P < 7.5 \text{ GPa}$, a typical characteristic of the material since it is a semiconductor. The slope of the temperature-dependent resistivity is positive, $d\rho/dT \geq 0$ for 16 GPa, a clear indication of metallization in our sample [40]. For pressures around 8 GPa, the $d\rho/dT$ is essentially temperature independent, suggesting that in our sample, there is a mixture of metal and semiconductor phases coexisting, as observed previously in other II-VI semiconductors [41]. Notice that this conclusion is consistent with Raman and XRD experiments which found a phase coexistence in the same pressure range.

In addition to the experiments, we performed *ab initio* calculations on the electronic structure of $\text{Cd}_{0.9}\text{Zn}_{0.1}\text{Te}$ at representative pressures to better understand the possible mechanism responsible for its highly tunable optical and electrical transport properties. At ambient pressure, the band gap E_g of $\text{Cd}_{0.9}\text{Zn}_{0.1}\text{Te}$ is direct with a value of 0.55 eV at the Γ point, as shown in Fig. 2(a). This value underestimates the experimental value by 1 eV, as the experimental value is 1.55 eV [34]. The underestimation of the calculated E_g is commonly observed in various DFT calculations. However, it usually gives a similar trend in the pressure dependence [42]. As shown in Fig. 2(d), E_g increases with pressure in the low-pressure region. On the other hand, the two HP phases of $\text{Cd}_{0.9}\text{Zn}_{0.1}\text{Te}$ are found to be metallic, as shown in Figs. 2(b) and 2(c). The metallization occurs at the ZB-RS transition through the closing of an indirect band gap. In the HP phases, we observed an increase in the width of the valence band and conduction band due to compression.

B. Pressure-induced structural changes from x-ray diffraction

High-pressure x-ray diffraction patterns were recorded up to 40 GPa. Structural changes are shown in Fig. 3(a) for a few representative pressures, and the index (hkl) of the Bragg peaks is marked for the ambient pressure phase. This phase has a cubic ZB structure that belongs to space group $F43m$. This space group is specified by the two interpenetrating face-centered-cubic (fcc) lattices offset from each other

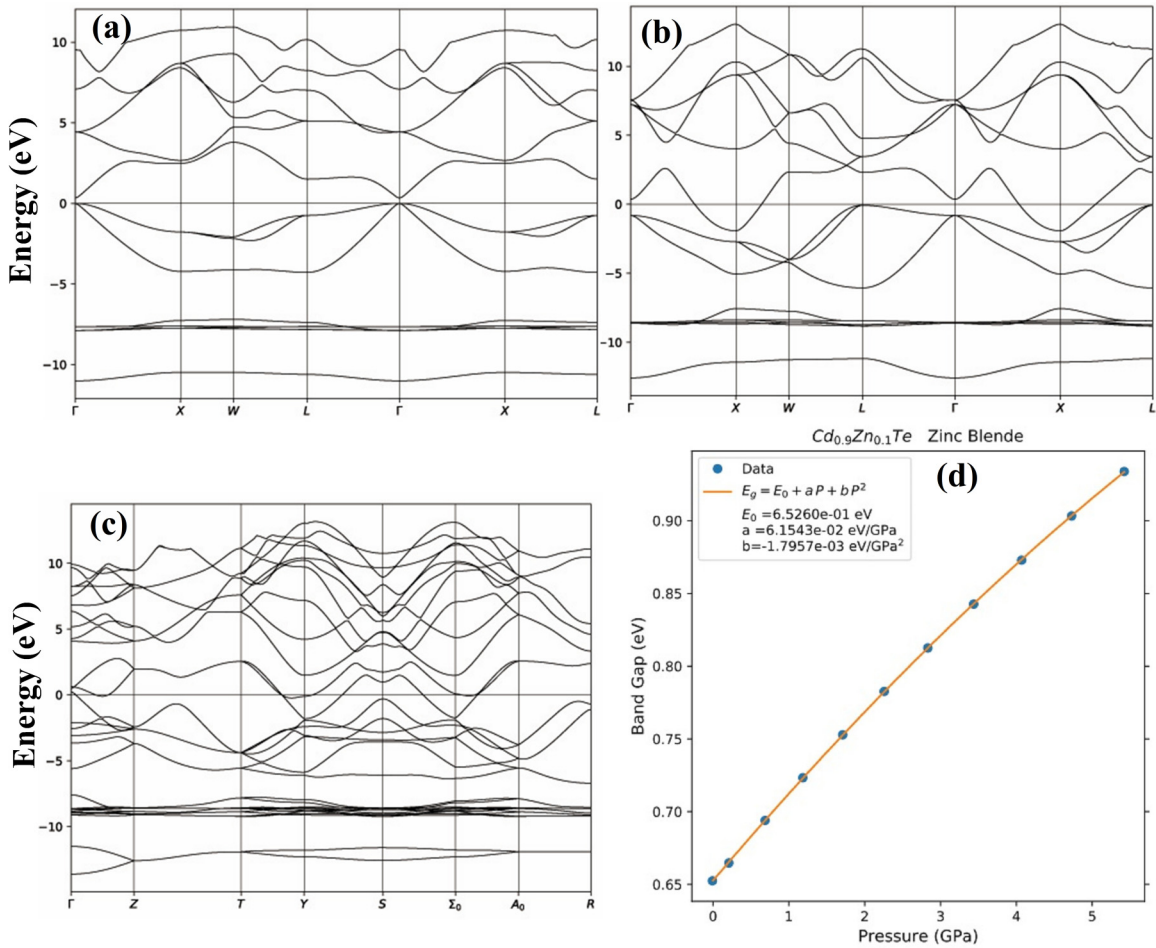


FIG. 2. Calculated band structure of $\text{Cd}_{0.9}\text{Zn}_{0.1}\text{Te}$ at (a) 0 GPa, (b) 7 GPa, and (c) 14 GPa for the ZB, RS, and $Cmcm$ structure, respectively. (d) Pressure dependence of the band gap in the LP region.

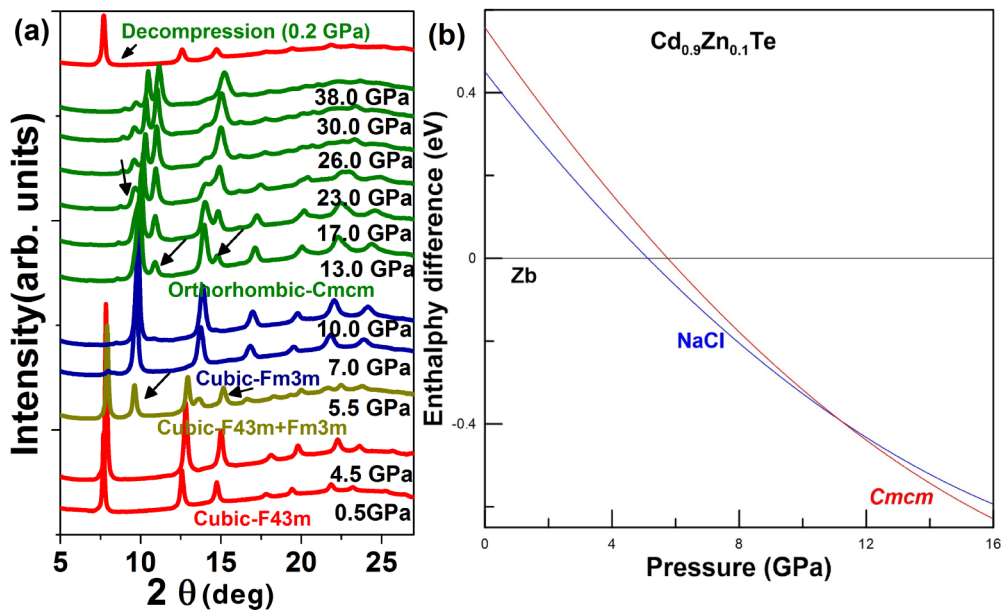


FIG. 3. (a) Angle-dispersive XRD patterns for $\text{Cd}_{0.9}\text{Zn}_{0.1}\text{Te}$ at selected pressures at room temperature ($\lambda = 0.4959 \text{ \AA}$). Arrows indicate the appearance of new peaks. (b) Pressure-dependent enthalpies of all three phases computed by first-principles calculations.

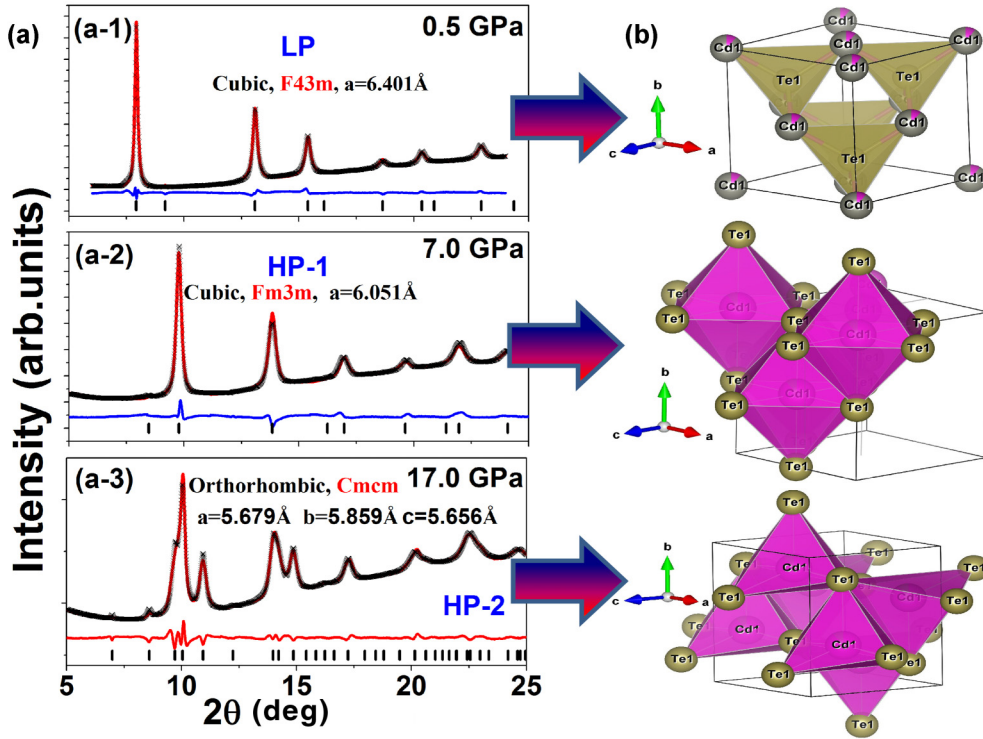


FIG. 4. (a) Rietveld refinements for the ambient pressure and new HP-1 and HP-2 phases at 7.0 and 17 GPa, respectively ($\lambda = 0.4959 \text{ \AA}$). (b) A comparison between the cubic- $F43m$, cubic- $Fm3m$, and orthorhombic- $Cmcm$ crystal structures.

by one-quarter of a unit cell body diagonal. This structure has tetrahedral coordination, such that each atom is surrounded by four close neighbor atoms belonging to the other fcc sublattice. Covalent bonding is established as a result of the sharing of four valence electrons by every atom with four neighboring atoms. The sample particle size obtained from scanning electron microscopy (SEM) agrees well with the calculated XRD data and is shown in Fig. S1 of the Supplemental Material [35]. Rietveld analysis provided the initial values of the cell parameters of the cubic structure, as illustrated in Fig. 4(a)(a-1) and Table I. The $\text{Cd}_{0.9}\text{Zn}_{0.1}\text{Te}$ retains the cubic $F43m$ structure up to 5.5 GPa, and the conductivity of the sample in this phase shows a linear increase. Between 0 to 5 GPa, no major change was found in the structure except a gradual shift of the Bragg peaks towards higher angles and small broadening for the specific high 2θ Bragg peaks after 2.5 GPa. The Bragg peaks shifted toward high angles due to the decrease of the unit-cell parameter, and peak broadening might be due to the nonhydrostatic conditions, cationic inversion, or a microstructural transition [43,44].

Above 5.5 GPa, five new diffraction peaks started to evolve at about 9.6° , 13.6° , 16.6° , 19.3° , and 21.6° (corresponding to d spacing 2.95 \AA , 2.09 \AA , 1.71 \AA , 1.47 \AA , 1.31 \AA), which indicate the appearance of a cubic $Fm3m$. We conclude that the low-pressure (LP) cubic- $F43m$ and HP-1 cubic- $Fm3m$ phases coexist between $5 < P < 7$ GPa, as shown in Fig. 3. At 7.5 GPa, cubic $F43m$ completely transforms to cubic $Fm3m$ with a lattice parameter $a = 6.051 \text{ \AA}$.

A huge volume collapse of about 18% is observed at this phase transition (see Fig. 5). Such a huge volume drop indicates the first-order nature of the phase transition. Our transport measurement results showed a sharp decrease in resistivity at the onset of this phase. The cubic- $Fm3m$ phase is also known as the RS phase, and it is stable up to 13 GPa. The crystal structure is shown in Fig. 4(b) and structural information is given in Table I. Upon slight compression, shoulders started to appear on the right side of the main diffraction peaks ((111) and (220)). These shoulders developed into visible peaks together with some other tiny peaks that grew in intensity with increasing pressure and, at about 13.5 GPa,

TABLE I. Lattice parameters and profile matching parameters of the cubic and high-pressure phases.

Phase	P	Lattice constant parameters			Z No.	Profile matching parameters		
		A	B	C		R_p	R_{wp}	χ^2
Cubic- $F43m$	0.5 GPa	6.40(1) \AA	6.40(1) \AA	6.40(1) \AA	4	1.18%	1.41%	0.97
Cubic- $Fm3m$	7.0 GPa	6.05 (2) \AA	6.05(2) \AA	6.05(2) \AA	4	1.41%	1.78%	1.62
Ortho- $Cmcm$	17 GPa	5.67(3) \AA	5.85(2) \AA	5.65(3) \AA	4	1.80%	1.93%	1.89

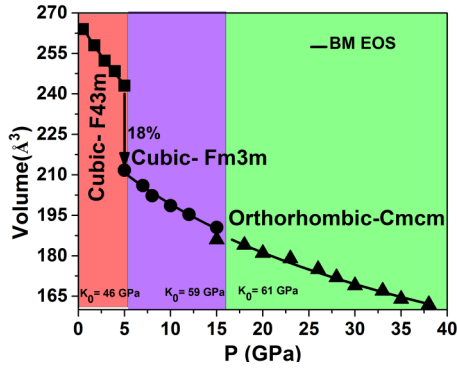


FIG. 5. Unit-cell volume as a function of pressure for cubic- $F4\bar{3}m$, cubic- $Fm\bar{3}m$, and orthorhombic- $Cmcm$ phase.

the onset of a new phase became apparent as the contribution of these additional peaks become more pronounced in the HP-XRD patterns.

Rietveld profile fittings of the patterns collected at both the ambient and HP phases are shown in Fig. 4. We tried to fit the HP-2 diffraction pattern of the new phase by employing different orthorhombic- and tetragonal-based subgroup considerations and preliminary models. We achieved reasonable fittings with orthorhombic ($Pnma$) and tetragonal ($Imm2$). However, the best agreement between the experimentally obtained pattern and the fitted profile was achieved when considering the subsequent refinements by the orthorhombic ($Cmcm$) space group as shown in Fig. 4(a)(a-3). More convincingly, the HP-2 phase is in good agreement with previous theoretical and experimental predictions [7,45]. The new diffraction peaks at 10.9° and 14.7° (corresponding to d spacing 2.6 \AA and 1.93 \AA) belong to an orthorhombic- $Cmcm$ structure, as illustrated in Fig. 3(a). Thus, the anticipated pressure for the HP-2 phase is $P \sim 13 \text{ GPa}$ ($\pm 2 \text{ GPa}$). The most dominant factor for this phase change is the site ordering, as supported by a previous study [7]. The distortion of the $Cmcm$ phase completed up to 26 GPa, as shown in Fig. 3. This orthorhombic- $Cmcm$ (HP-2) phase exhibits metallic behavior, as shown in Fig. 1 and Fig. 2. Hence, we have a self-consistent explanation of the high electrical conductivity of the HP-2 phase.

The profile matching parameters and lattice constant parameters of both high-pressure phases (HP-1, HP-2) obtained from the full-profile Rietveld refinements are given in Figs. 4(a)(a-2), 4(a)(a-3), and Table I. This pressure-induced cubic- $Fm\bar{3}m$ to orthorhombic- $Cmcm$ phase transition involves an increase of the material density by approximately 2% as a result of the volume change. The volume discontinuity can be seen in Fig. 5.

From ambient pressure to nearly 40 GPa, the unit cell undergoes a decrease in volume of nearly 40%. With the decrease of the unit-cell size, valence electrons of neighboring atoms are getting closer and closer, leading to enhanced overlap of electron wave functions. As a result, previously localized electronic states become delocalized and electric conductivity increases. At phase transformation pressures near 5 and 13 GPa, the wave-function overlap undergoes a sudden enhancement due to the abrupt volume decrease. The unit-cell volume for the cubic- $F4\bar{3}m$, cubic- $Fm\bar{3}m$,

and orthorhombic- $Cmcm$ phases decreases continuously as a function of pressure. The pressure-volume data were fitted with the third-order Birch-Murnaghan equation of state (BM-EOS) [46] to determine the elastic parameters:

$$P = \frac{3}{2}K_0[(V_0/V)^{7/3} - (V_0/V)^{5/3}] \times \{1 - (3/4)(4 - K'_0)[(V_0/V)^{2/3} - 1]\}, \quad (1)$$

where P and V are the measured pressure and unit-cell volume, respectively. K_0 is the bulk modulus, K'_0 is the first pressure derivative of the bulk modulus, and V_0 is the unit-cell volume at ambient conditions. Calculations give $K_0 = 46(4) \text{ GPa}$, $K'_0 = 4.2(5)$, $V_0 = 270(5) \text{ \AA}^3$ for the LP cubic phase, $K_0 = 59(5) \text{ GPa}$, $K'_0 = 4.2(4)$, $V_0 = 262(6) \text{ \AA}^3$ for the HP-1 cubic phase, and $K_0 = 61(5) \text{ GPa}$, $K'_0 = 4.2(4)$, $V_0 = 236(6) \text{ \AA}^3$ for the HP-2 orthorhombic phase. These values illustrate that both phases (HP-1 and HP-2) have similar compressibility. The bulk modulus and its pressure derivative for $\text{Cd}_{0.9}\text{Zn}_{0.1}\text{Te}$ determined in this study are also consistent with a previous study of similar compounds, shown in Table S2 of the Supplemental Material [35]. We note that the decompression process leads to the appearance of the initial $F4\bar{3}m$ structure, as shown in Fig. 3. The variation of experimentally determined lattice parameters of $\text{Cd}_{0.9}\text{Zn}_{0.1}\text{Te}$ with P at RT for all diffraction patterns is summarized in Table I.

Ab initio calculations were carried out to understand the phase transformation of $\text{Cd}_{0.9}\text{Zn}_{0.1}\text{Te}$ under pressure. The computed enthalpy curves based on first-principles calculations are shown in Fig. 3(b). We found the cubic ZB phase was the most stable at ambient conditions, and the cubic RS became the most stable phase at 5.5 GPa [see Fig. 3(b)]. This is in agreement with the structural sequence found in the experiments. The calculated unit-cell parameter of the ZB phase at 0 GPa is $a = 6.4827 \text{ \AA}$. Our RS phase obtained at 5.5 GPa has $a = 6.0943 \text{ \AA}$. The second transition to the $Cmcm$ phase is found at 13 GPa. These transition points are in good agreement with the experimentally observed pressure values. The lattice parameters of our predicted HP-2 phase obtained at 13 GPa are $a = 5.5730 \text{ \AA}$, $b = 5.9603 \text{ \AA}$, and $c = 5.5840 \text{ \AA}$. The agreement between the calculated and measured structures gives reliability to the proposed structural sequence.

C. Pressure-dependent Raman spectroscopy

In order to study the lattice dynamics of $\text{Cd}_{0.9}\text{Zn}_{0.1}\text{Te}$ under pressure, we recorded Raman spectra as a function of P in the range of $100 - 400 \text{ cm}^{-1}$, as shown in Fig. 6(a). The ideal cubic $\text{Cd}_{0.9}\text{Zn}_{0.1}\text{Te}$ has three active modes: A1 (Te), TO (CdTe), and LO (CdTe), labeled as M1, M2, and M3, respectively. Our calculations also predicted M2 and M3 modes and the results agree with previous results [47]. The presence of defects, interstitial cations, and vacancies may result in the activation of other phonon modes that are not predicted by group theory. The lowest-frequency mode M1 is the phonon with A1 symmetry of Te inclusions in $\text{Cd}_{1-x}\text{Zn}_x\text{Te}$, while the other two modes are due to the presence of CdTe. The M3 mode is the lower intensity mode that was not clearly observed in ambient spectra. The spectrum recorded at 0.5 GPa is deconvoluted into three independent Lorentzian peaks, as shown in Fig. 6(b). We observed the M3 mode clearly along

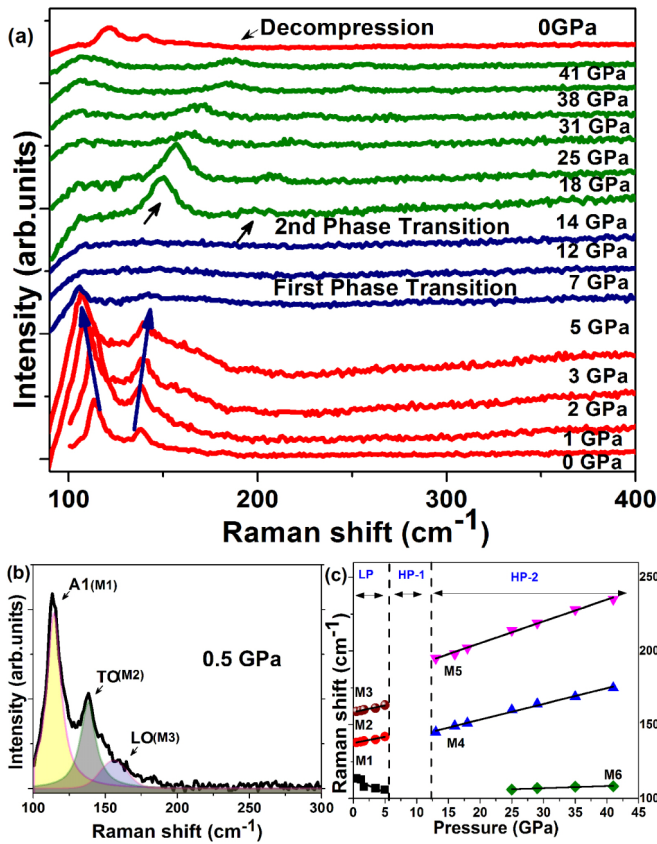


FIG. 6. (a) Raman spectra of $\text{Cd}_{0.9}\text{Zn}_{0.1}\text{Te}$ from 0 to 40 GPa showing Raman modes disappearing at the first phase transition (HP-1) and reappearing modes at the second phase transition (HP-2). (b) Deconvoluted spectra with Lorentzian fitting for the Raman modes at 0.5 GPa. (c) Pressure dependence of the Raman modes at different pressures from 0 and 40 GPa, where solid lines show the linear fits corresponding to the specific modes.

with a photoluminescence peak (at 183 cm^{-1}) by using a 785 nm laser excitation. Details of the HP Raman spectra using the 785 nm laser excitation are discussed in the Supplemental Material [35].

The Raman modes of the $\text{Cd}_{0.9}\text{Zn}_{0.1}\text{Te}$ for the $F4\bar{3}m$ phase do not show normal behavior during pressure increase. In the present study, we observed the following: (i) softening and hardening of M1, M2, and M3, respectively, with an increase of pressure; (ii) complete disappearance of the Raman modes beyond 5 GPa; and (iii) appearance of new Raman modes M4, M5, and M6 beyond 13 GPa.

Mode softening is found for the peak M1 with a lower frequency, whereas the Raman shift increases with pressure for the higher-frequency components M2 and M3. The sign of the pressure dependence of the phonon frequencies in tetrahedral semiconductors depends on a balance between central and noncentral elastic forces associated with the stretching and bending of bonds. For the shear-type zone-boundary TA modes, the angular forces tend to make the mode stiffer under pressure, but central elastic forces act oppositely, resulting in a mode softening [48]. Mode softening observed in tetrahedrally coordinated compounds has been speculated to be responsible for driving the phase transition [49]. Further

compression leads to the disappearance of all Raman modes after 5 GPa. The disappearance of Raman signals is usually associated with some structural transition and/or conductivity changes. We attribute this change to the structural transition from the ZB to the RS phase. For the RS phase, first-order Raman scattering is forbidden by the selection rules and, hence, the phase transition is accompanied by the vanishing Raman modes. Our DFT calculations give similar frequencies and pressure coefficients as observed in experiments (see Table S1 of the Supplemental Material) [35].

At $P \geq 13$ GPa in the vicinity of a cubic-orthorhombic phase transition, new Raman modes M4 and M5 reappeared at 146 and 195 cm^{-1} , respectively. The M6 mode was clearly visible beyond 25 GPa. In light of the XRD results, at the first transition, the system transformed into a higher-symmetry structure that involved the disappearance of all Raman modes in this region. However, for the second transition to the orthorhombic phase, which has lower symmetry than the cubic phase, we observed the appearance of new Raman modes. All new Raman modes shifted to a higher wave number with increasing pressure. Notice that calculations predict the existence of six Raman-active modes in this structure. However, since the nature of the orthorhombic $Cmcm$ has been concluded to be metallic, the Raman signal should be extremely weak [22], as found in our studies. In particular, in this orthorhombic metallic phase, definite Raman modes are discerned, in comparison to the preceding RS metallic phase where no Raman modes are observed. Based on calculations, we have confirmed that three Raman modes (M4, M5, and M6) belong to the orthorhombic phase of $\text{Cd}_{0.9}\text{Zn}_{0.1}\text{Te}$. The rest of the modes were not detected because they are expected at lower frequencies than those measured with our setup. After the release of P , some of the Raman modes return to ambient conditions, indicating that the phase transition is reversible.

The pressure dependence of Raman frequency shifts is plotted in Fig. 6(c), where considerable changes of $d\omega/dP$ have been marked by the dotted lines at 5 and 13 GPa. The detailed analysis shows that with increasing pressure, all phonon modes shift to higher frequencies linearly for the LP, HP-1, and HP-2 phases, except the M1 modes where $d\omega/dP < 0$. The Grüneisen parameter of the low-pressure region and high-pressure regions is calculated and shown in Table II.

Using the bulk modulus (K_0) determined from the x-ray diffraction data, the mode-Grüneisen parameters (γ) were obtained from the following equation: $\gamma = K_0/\omega_0(d\omega/dP)$ where ω_0 , P , and $d\omega/dP$ are the frequency of the Raman shift observed at 1 atm, the applied pressure, and pressure-dependent frequency shift of Raman modes, respectively. The assignment of all Raman modes in $\text{Cd}_{0.9}\text{Zn}_{0.1}\text{Te}$ is listed in Table II along with a summary of the frequencies ω_0 , pressure coefficient, and Grüneisen parameter γ of the different modes. The values of the Grüneisen parameters for the cubic LP and HP orthorhombic phases range from -0.72 to 0.28 and from 0.59 to 0.24 , respectively, and are consistent with previous work [50]. The obtained mode Grüneisen parameters can be used to determine the heat capacities and vibrational entropies using the Kieffer model [51].

We also calculated the vibrational phonon frequencies of the predicted HP-2 $Cmcm$ phase by theoretical analysis. A

TABLE II. Observed Raman modes, pressure coefficients ($d\omega/dP$), and calculated Grüneisen parameters of $\text{Cd}_{0.9}\text{Zn}_{0.1}\text{Te}$.

Low-pressure cubic phase				High-pressure orthorhombic phase			
Raman modes ω (cm^{-1})	$d\omega/dP$ ($\text{cm}^{-1}/\text{GPa}$)	γ	Mode	Observed modes ω_o (cm^{-1})	$d\omega/dP$ ($\text{cm}^{-1}/\text{GPa}$)	γ	
115	-1.83	-0.72	M1	131.9	1.06	0.49	
137	0.85	0.28	M2	175.6	1.47	0.59	
158	0.852	0.284	M3	102.6	0.41	0.24	

good agreement was found in the theoretical and calculated values for the mode frequencies. The details of this analysis and a comparison of the experimental and calculated values are provided in the Supplemental Material [35].

IV. DISCUSSION

Our XRD experiment illustrates a cubic- $F4\bar{3}m$ (ZB) to cubic- $Fm\bar{3}m$ (RS) phase transition for $\text{Cd}_{0.9}\text{Zn}_{0.1}\text{Te}$ at 5.5 GPa, while a second transition to an orthorhombic- $Cmcm$ phase was observed at 13 GPa. The reliability of the occurrence of such polymorphic behavior under pressure is consistent with previous and present experimental as well as theoretical studies of various tetrahedral coordinated (IIB-VIA) compounds [8,52,53]. Our observed XRD spectra also did not reveal any discontinuity before the ZB-RS phase transition as found for the parent compound in previous studies [19,20]. This could be due to the nanoparticle size of the sample used [54].

Other similar materials such as SnTe and ZnSe are transformed directly from a ZB to a RS phase and are further transformed to an orthorhombic structure at higher pressures [55,56]. Our first phase transition involved an abrupt volume collapse of about 18%. Similar large volume collapses have been reported in other tetrahedral coordinated compounds; for example, Yao *et al.* and Strassner *et al.* reported a similarly large volume collapse in chalcogenide compounds due to a ZB-RS phase transition [56,57].

Our observed phase transition from RS to $Cmcm$ at 13 GPa agrees with the HP phase reported in many compounds. Nelmes *et al.* reported in their diverse studies that orthorhombic-type low-symmetry structures are dominant at high pressure for various group II-VI compounds [53]. Our XRD result reveals a transition from RS to the $Cmcm$ phase with a relatively smaller volume change of about 2%, similar to the reported transition for CdTe [7]. Our transport measurement reveals an overall drop of 11 orders of magnitude of resistivity, of which a sharp six-order drop was seen at the first transition point. Such a large drop in resistivity is associated with a phase transition to the RS phase. He *et al.* measured the resistivity of bulk CdTe under HP and attributed the anomalous decrease in the resistivity of five orders to the structural phase transitions to RS and $Cmcm$ structures, respectively [23]. Such drastic changes in resistivity for semiconducting $\text{Cd}_{0.9}\text{Zn}_{0.1}\text{Te}$ can be related to the carrier concentrations as we have calculated against both the ambient LP and HP-2 phases, respectively. Since $\text{Cd}_{0.9}\text{Zn}_{0.1}\text{Te}$ is an extrinsic semiconductor, our observed resistivity changes can be considered to be the direct consequence of variations in carrier concentration. We can also refer to the Hall effect

measurement results for single-crystal CdTe by Errandonea *et al.* for a deeper interpretation of our resistivity changes [22]. Hence a dominant effect producing the decrease in resistivity at the onset of the ZB-RS phase is an increase in the carrier concentration, in addition to the changes in the band structure. A carrier density of 10^{22}cm^{-3} seen after a phase transition is considered to be extrinsic in origin [22]. Further resistivity change was observed at the $Cmcm$ phase. Our temperature-dependent resistivity data confirmed the metallic behavior of both the RS and $Cmcm$ phase. The $d\rho/dT$ is independent of temperature for pressures 8 GPa, while $d\rho/dT$ becomes positive at 16 GPa. The conducting nature of the $Cmcm$ phase in the parent compound is proved to be metallic in various reports based on experimental and theoretical measurements. However, in our present study, metallic behavior started at lower pressure in the HP-1 phases. Guder *et al.* calculated the electronic structures of CdTe at different pressures and showed that at 10 GPa, the shrinking and disappearance of the transparency region occurred as a result of a phase transition to the metallic $Cmcm$ phase [38]. Based on the Hall effect measurements, Errandonea *et al.* confirmed the metallic nature of the $Cmcm$ phase for the parent CdTe compound [22]. However, our current study suggests an efficient way of getting a large conductivity increase at about 8.5 GPa. Our Raman spectra revealed the disappearance of Raman modes related to a phase transition above 5.5 GPa, while some Raman signals reappeared beyond 12 GPa. Such reappearance of Raman modes has not been reported in earlier studies of similar compounds. We consider the vanishing Raman signals to be the effect of a phase transition to the RS phase. Arora *et al.* reported the disappearance of Raman modes at the phase transition from the ZB phase to RS phase in a mixed crystal of $\text{Cd}_{1-x}\text{Mn}_x\text{Te}$ [58]. HP Raman spectra of ZnTe do not show Raman signals disappearing where the transition sequence for ZnTe involves the direct transition from a Cinnabar phase to a $Cmcm$ phase without passing through RS [59]. The transition pressure for the $\text{Cd}_{0.90}\text{Zn}_{0.10}\text{Te}$ samples seen in our study is higher than the respective onset phase transition pressures for the parent compound CdTe [7,18], but our resistivity drop is at a lower pressure than previous studies of the parent compound. Most importantly, the 11-order drop of resistivity has not been observed in a similar class of compound. For mixed crystals, the influence of substitution on the transition pressure has been discussed in various reports [60]. A HP study by Alain *et al.* suggested an increase in transition pressure by increasing the amount of constituent, for $\text{Zn}_x\text{Cd}_{1-x}\text{S}$ alloys [61]. Enhanced transition pressure can be attributed to the improved stability of the $\text{Cd}_{0.9}\text{Zn}_{0.1}\text{Te}$ crystal [62]. The dislocation energies in semiconductors

are proportional to the reciprocal of the ninth power of the nearest-neighbor bond length. This explains the reason for a greater strength of the $\text{Cd}_{1-x}\text{Zn}_x\text{Te}$ crystal where a small percentage of Zn atoms is added to Cd atoms in the parent compound CdTe to reduce the dislocation density. Findings of this work may stimulate further exploration of this material for new applications in industries.

V. CONCLUSION

In summary, we systematically explored the electronic and structural properties of $\text{Cd}_{0.90}\text{Zn}_{0.10}\text{Te}$ under high pressure using resistivity measurements, x-ray diffraction, Raman spectroscopy, and DFT calculations. A transition from the ambient phase cubic- $F43\bar{m}$ to a cubic- $F\bar{m}3m$ phase (HP-1) was observed by x-ray diffraction at 5.5 GPa. The transition was confirmed by the disappearance of the Raman signals. In addition, the resistivity dropped sharply at this transition. Another phase transition from the cubic- $F\bar{m}3m$ to an orthorhombic- $Cmcm$ (HP-2) structure was observed at

13 GPa. Beyond this pressure, the resistivity became constant with a further decrease in resistivity. Metallic behavior was determined for both the HP-1 and HP-2 phases through the temperature-dependent resistivity and *ab initio* calculations. The phase transitions were associated with large crystal volume shrinkage. The enhanced conductivity was attributed to the band structure changes as well as the rapid increase in carrier concentration.

ACKNOWLEDGMENTS

Some of the authors are thankful for the financial support of the Spanish Ministerio de Ciencia, Innovación y Universidades, the Spanish Research Agency (AEI), the European Fund for Regional Development (FEDER) under Grant No. MAT2016-75586-C4-1/3-P, and by Generalitat Valenciana under Grant Prometeo/2018/123 (EFIMAT), the National Natural Science Foundation in China (Grant No. 61290304), and the Frontier Science Research Project (Key Programs) of Chinese Academy of Sciences (Grant No. QYZDJ-SSW-SLH018).

-
- [1] S. Z. Karazhanov, P. Ravindran, A. Kjekshus, H. Fjellvåg, and B. G. Svensson, *Phys. Rev. B* **75**, 155104 (2007).
- [2] W. W. Koelmans, A. Sebastian, V. P. Jonnalagadda, D. Krebs, L. Dellmann, and E. Eleftheriou, *Nat. Commun.* **6**, 8181 (2015).
- [3] S. LeBlanc, *Sustainable Mater. Technol.* **1-2**, 26 (2014).
- [4] P. D. Antunez, J. J. Buckley, and R. L. Brutchey, *Nanoscale* **3**, 2399 (2011).
- [5] I. Khan, H. A. R. Aliabad, W. Ahmad, Z. Ali, and I. Ahmad, *Superlattices Microstruct.* **63**, 91 (2013).
- [6] Y. Zhang, Y. Chang, Z. Song, T. Zhang, Q. Liu, H. Zhong, and Y. Jiang, *J. Alloys Compd.* **712**, 543 (2017).
- [7] R. J. Nelmes, M. I. McMahon, N. G. Wright, and D. R. Allan, *Phys. Rev. B* **51**, 15723 (1995).
- [8] R. J. Nelmes, M. I. McMahon, N. G. Wright, and D. R. Allan, *Phys. Rev. Lett.* **73**, 1805 (1994).
- [9] X. Cui, T. Hu, J. Yang, Y. Han, Y. Li, C. Liu, Y. Wang, B. Liu, W. Ren, N. Su, H. Liu, and C. Gao, *Physica Status Solidi (c)* **8**, 1676 (2011).
- [10] A. San-Miguel, A. Polian, M. Gauthier, and J. P. Itié, *Phys. Rev. B* **48**, 8683 (1993).
- [11] L. Kranz, C. Gretener, J. Perrenoud, R. Schmitt, F. Pianezzi, F. La Mattina, P. Blösch, E. Cheah, A. Chirilă, C. M. Fella, H. Hagendorfer, T. Jäger, S. Nishiwaki, A. R. Uhl, S. Buecheler, and A. N. Tiwari, *Nat. Commun.* **4**, 2306 (2013).
- [12] S. Ebrahim, W. Ramadan, and M. Ali, *J. Mater. Sci.: Mater. Electron.* **27**, 3826 (2016).
- [13] R. Weil, R. Nkum, E. Muranevich, and L. Benguigui, *Phys. Rev. Lett.* **62**, 2744 (1989).
- [14] O. Adegoke and E. Y. Park, *Sci. Rep.* **6**, 27288 (2016).
- [15] Y. Wang, G. Ouyang, L. L. Wang, L. M. Tang, D. S. Tang, and C. Q. Sun, *Chem. Phys. Lett.* **463**, 383 (2008).
- [16] L. F. Voss, A. M. Conway, A. J. Nelson, P. R. Beck, R. T. Graff, R. J. Nikolic, S. A. Payne, A. Burger, and H. Chen, *IEEE Trans. Nucl. Sci.* **60**, 1208 (2013).
- [17] S. N. Garaje, S. K. Apte, S. D. Naik, J. D. Ambekar, R. S. Sonawane, M. V. Kulkarni, A. Vinu, and B. B. Kale, *Environ. Sci. Technol.* **47**, 6664 (2013).
- [18] M. I. McMahon, R. J. Nelmes, N. G. Wright, and D. R. Allan, *Phys. Rev. B* **48**, 16246 (1993).
- [19] A. N. Mariano and E. P. Warekois, *Science* **142**, 672 (1963).
- [20] R. J. Nelmes, M. I. McMahon, N. G. Wright, and D. R. Allan, *Phys. Rev. B* **48**, 1314 (1993).
- [21] S. Gilliland, J. González, H. S. Güder, A. Segura, I. Mora, and V. Muñoz, *Physica Status Solidi (b)* **235**, 441 (2003).
- [22] D. Errandonea, A. Segura, D. Martínez-García, and V. Muñoz-San Jose, *Phys. Rev. B* **79**, 125203 (2009).
- [23] H. Chun-Yuan, G. Chun-Xiao, L. Ming, H. Ai-Min, H. Xiao-Wei, Z. Dong-Mei, Y. Cui-Ling, and W. Yue, *Chin. Phys. Lett.* **24**, 1070 (2007).
- [24] E. Diéguez, in *Comprehensive Semiconductor Science and Technology*, edited by R. Fornari and H. Kamimura (Elsevier, Amsterdam, 2011), p. 170.
- [25] J. Yang, G. Peng, C.-L. Liu, H. Lu, Y.-H. Han, and C.-X. Gao, *Chin. Phys. Lett.* **30**, 060701 (2013).
- [26] H. K. Mao, J. Xu, and P. M. Bell, *J. Geophys. Res.: Solid Earth* **91**, 4673 (1986).
- [27] J. Rodríguez-Carvajal, *Physica B: Condens. Matter* **192**, 55 (1993).
- [28] P. Hohenberg and W. Kohn, *Phys. Rev.* **136**, B864 (1964).
- [29] X. Gonze, B. Amadon, P. M. Anglade, J. M. Beuken, F. Bottin, P. Boulanger, F. Bruneval, D. Caliste, R. Caracas, M. Côté, T. Deutsch, L. Genovese, P. Ghosez, M. Giantomassi, S. Goedecker, D. R. Hamann, P. Hermet, F. Jollet, G. Jomard, S. Leroux, M. Mancini, S. Mazevet, M. J. T. Oliveira, G. Onida, Y. Pouillon, T. Rangel, G. M. Rignanese, D. Sangalli, R. Shaltaf, M. Torrent, M. J. Verstraete, G. Zerah, and J. W. Zwanziger, *Comput. Phys. Commun.* **180**, 2582 (2009).
- [30] M. Fuchs and M. Scheffler, *Comput. Phys. Commun.* **119**, 67 (1999).
- [31] J. P. Perdew, K. Burke, and M. Ernzerhof, *Phys. Rev. Lett.* **77**, 3865 (1996).
- [32] H. J. Monkhorst and J. D. Pack, *Phys. Rev. B* **13**, 5188 (1976).
- [33] K. Parlinski, computer code PHONON, <http://www.computingformaterials.com/> (unpublished).

- [34] S. Del Sordo, L. Abbene, E. Caroli, A. M. Mancini, A. Zappettini, and P. Ubertini, *Sensors* **9**, 3491 (2009).
- [35] See Supplemental Material at <http://link.aps.org/supplemental/10.1103/PhysRevB.99.094109> for (i) SEM images of Cd_{0.90}Zn_{0.1}Te sample, (ii) verification of Zn concentration in Cd_{0.90}Zn_{0.1}Te, (iii) particle size Cd_{0.90}Zn_{0.1}Te, (iv) calculated LP and HP Raman modes, (v) details of the HP Raman spectra using the 785 nm laser excitation, (vi) comparison of bulk moduli with other telluride systems, and (vii) pressure-dependent I-V behavior.
- [36] D. Errandonea, A. Segura, F. J. Manjón, and A. Chevy, *Semicond. Sci. Technol.* **18**, 241 (2003).
- [37] N. E. Christensen and O. B. Christensen, *Phys. Rev. B* **33**, 4739 (1986).
- [38] H. S. Güder, S. Gilliland, J. A. Sans, A. Segura, J. González, I. Mora, V. Muñoz, and A. Muñoz, *Physica Status Solidi (b)* **235**, 509 (2003).
- [39] J. C. Erickson, H. W. Yao, R. B. James, H. Hermon, and M. Greaves, *J. Electron. Mater.* **29**, 699 (2000).
- [40] C.-M. Lin, K.-L. Lin, Y.-K. Chern, Y.-K. Lin, Y.-C. Chuang, Y.-F. Liao, Y.-W. Suen, S.-R. Jian, and J.-Y. Juang, *Sci. Adv. Mater.* **7**, 1039 (2015).
- [41] G. Itkin, G. R. Hearne, E. Sterer, M. P. Pasternak, and W. Potzel, *Phys. Rev. B* **51**, 3195 (1995).
- [42] J. Ruiz-Fuertes, S. López-Moreno, J. López-Solano, D. Errandonea, A. Segura, R. Lacomba-Perales, A. Muñoz, S. Radescu, P. Rodríguez-Hernández, M. Gospodinov, L. L. Nagornaya, and C. Y. Tu, *Phys. Rev. B* **86**, 125202 (2012).
- [43] D. Errandonea, *Cryst. Res. Technol.* **50**, 729 (2015).
- [44] D. Errandonea, Y. Meng, M. Somayazulu, and D. Häusermann, *Physica B: Condens. Matter* **355**, 116 (2005).
- [45] S. Mnasri, S. A.-B. Nasrallah, N. Sfina, N. Bouarissa, and M. Said, *Semicond. Sci. Technol.* **24**, 095008 (2009).
- [46] E. Greenberg, G. K. Rozenberg, W. Xu, R. Arielly, M. P. Pasternak, A. Melchior, G. Garbarino, and L. S. Dubrovinsky, *High Pressure Res.* **29**, 764 (2009).
- [47] P. M. Amirtharaj and F. H. Pollak, *Appl. Phys. Lett.* **45**, 789 (1984).
- [48] C. H. Xu, C. Z. Wang, C. T. Chan, and K. M. Ho, *Phys. Rev. B* **43**, 5024 (1991).
- [49] N. J. Walker, G. A. Saunders, and J. E. Hawkey, *Philos. Mag.* **52**, 1005 (1985).
- [50] T. F. Smith and G. K. White, *J. Phys. C: Solid State Phys.* **8**, 2031 (1975).
- [51] S. W. Kieffer, *Rev. Geophys.* **17**, 1 (1979).
- [52] A. Werner, H. D. Hochheimer, K. Strössner, and A. Jayaraman, *Phys. Rev. B* **28**, 3330 (1983).
- [53] R. J. Nelmes, M. I. McMahon, N. G. Wright, and D. R. Allan, *J. Phys. Chem. Solids* **56**, 545 (1995).
- [54] A. San-Miguel, *Chem. Soc. Rev.* **35**, 876 (2006).
- [55] D. Zhou, Q. Li, Y. Ma, Q. Cui, and C. Chen, *J. Phys. Chem. C* **117**, 5352 (2013).
- [56] L. D. Yao, F. F. Wang, X. Shen, S. J. You, L. X. Yang, S. Jiang, Y. C. Li, K. Zhu, Y. L. Liu, A. L. Pan, B. S. Zou, J. Liu, C. Q. Jin, and R. C. Yu, *J. Alloys Compd.* **480**, 798 (2009).
- [57] K. Strössner, S. Ves, W. Dieterich, W. Gebhardt, and M. Cardona, *Solid State Commun.* **56**, 563 (1985).
- [58] A. K. Arora, D. U. Bartholomew, D. L. Peterson, and A. K. Ramdas, *Phys. Rev. B* **35**, 7966 (1987).
- [59] J. Camacho, I. Loa, A. Cantarero, and K. Syassen, *High Pressure Res.* **22**, 309 (2002).
- [60] C. S. Yang, C. S. Ro, W. C. Chou, C. M. Lin, D. S. Chuu, J. Hu, E. Huang, and J. Xu, *J. Appl. Phys.* **85**, 8092 (1999).
- [61] A. Béliveau and C. Carlone, *Phys. Rev. B* **44**, 3650 (1991).
- [62] S. B. Qadri, E. F. Skelton, A. W. Webb, and J. Kennedy, *Appl. Phys. Lett.* **46**, 257 (1985).